

Introducing the pro-coagulant contact system in the numerical assessment of device-related thrombosis

Rodrigo Méndez Rojano · Simon Mendez · Franck Nicoud

Received: date / Accepted: date

Abstract Thrombosis is a major concern in blood-coated medical devices. Contact activation, which is the initial part of the coagulation cascade in device-related thrombosis, is not considered in current thrombus formation models. In the present study, pro-coagulant reactions including the contact activation system are coupled with a fluid solver. The biochemical/fluid model is applied to a backward facing step configuration, a flow configuration that frequently appears in medical devices. **The objective of this study is to evaluate the potential of the contact system to initiate thrombin production; for this reason the role of the anionic phospholipids (platelet activity), fibrin formation and fluid-structure interaction of a growing thrombus were neglected.** In contrast to the in vivo thrombosis models in which a specific thrombotic zone (injury region) is set a priori by the user to initiate the coagulation reaction, a reactive surface boundary condition is applied to the whole device wall. Simulation results show large thrombin concentration in regions related to recirculation zones without the need of an a priori knowledge of the thrombus location. The numerical results align well with the regions prone to thrombosis observed in experimental results reported in the literature. **This type of approach could complement thrombus formation models that take into account platelet activity and thrombus deposition that could contribute to optimize a wide range of medical devices.**

Keywords Thrombosis · Medical devices · Contact System · Hemodynamics

Rodrigo Méndez Rojano · Simon Mendez · Franck Nicoud
Institut Montpellierain Alexander Grothendieck,
CNRS, Univ. Montpellier
2 Place Eugène Bataillon, 34095 Montpellier Cedex 5, France
E-mail: rodrigo.mendez-rojano@umontpellier.fr

1 Introduction

The use of blood-coated devices is a common medical practice to treat several cardiovascular conditions. However, the poor thrombotic performance of some types of medical devices remains an issue in clinical practice (Chan et al (2009); Mehra et al (2014); Hastings et al (2017)). For instance, thrombus formation may lead to device malfunction, thrombo-embolism or increased risk of a hemorrhagic stroke due to the anti-coagulant therapy. Thrombosis is a complex phenomenon that involves several processes such as coagulation reactions, platelet activation/aggregation, blood flow dynamics, among others. Furthermore, these mechanisms interact with each other at different time and spatial scales as explained in Furie and Furie (2008). When it comes to device-related thrombosis, the artificial wall of the device interacts with the thrombotic processes as pointed out by Gorbet and Sefton (2004). Wall protein adsorption (Vroman effect) drives contact activation that initiates the coagulation reactions. At the same time, platelets adhesion and activation take place (Jaffer et al (2015)), constituting the platelet-fibrin clot that will form the stable thrombus.

In recent studies, computational fluid dynamics has been used to predict the flow in medical devices, with the long-term objective of improving their thrombotic performance (Alemu et al (2010); Piatti et al (2015)). However, most of the thrombus formation models are dedicated to **platelet activity and in-vivo situations in which no medical device is present.** Numerical studies that **consider platelet activity focused in characterizing the mechanical activation of platelets (Hellums (1994); Kroll et al (1996); Jetsy et al (2003); Nobili et al (2008); Shadden and Hendabadi (2013)).** In contrast, **in-vivo models** are based on a series of reaction equations modeling

the coagulation cascade, from the exposure of tissue factor to the generation of thrombin (Sorensen et al (1999); Kuharsky and Fogelson (2001); Fogelson and Guy (2008); Anand et al (2008); Seo et al (2016); Yazdani et al (2017)). Generally, in vivo models, prescribe an injury zone determined by the user producing tissue factor and thus, initiating the coagulation reactions (Biasseti et al (2012); Seo et al (2016)). This type of approach cannot be used for device-related thrombosis due to the lack of a priori knowledge of the thrombotic zone. For this reason, the models dedicated to evaluate the device thrombotic performance have focused on platelet activity. For instance, Goodman et al (2005) developed a model to predict device-induced thrombosis based on platelet activation (agonist induced platelet activation as in Sorensen et al (1999) and mechanical platelet activation by shear stress). Furthermore, the model accounts for platelet adhesion to artificial surfaces and thrombus growth by substantially increasing the fluid viscosity. Taylor et al (2016) developed a macroscopic model that includes platelet activation and thrombus growth in regions related to high and low wall shear stress (WSS), respectively. Their model was derived from the work of Fogelson (1992) with some modifications to account for device-related thrombosis. While platelet activity has been extensively considered, other major players like the complement and contact activation systems must be included in the modeling, as pointed out by Gorbet and Sefton (2004). Moreover, considering contact activation could provide significant information to platelet models since one mechanism of their activation is due to thrombin as explained in Fogelson and Neeves (2015), the latter being partially produced by reactions initiated by the contact system (Larsson et al (2014)). To the best of our knowledge, the only model considering the interaction of an idealized flow configuration and the contact activation system is the one of Gregory and Basmadjian (1994). In their work, a steady-state solution of a kinetic model is analyzed. The coagulation reactions in this model include contact activation of factor XII and the common pathway of the coagulation cascade (until factor XI_a). The model results showed significant sensitivity to the flow dynamics and surface activity. A more recent kinetic model that considers the contact system in a platelet plasma kinetic network was developed by Chatterjee et al (2010). Their model predicts the coagulation time of quiescent human blood samples without the action of tissue factor (TF). The results show that coagulation is due to the combined action of factors $XIII_a$ and XI_a . In parallel, recent clinical studies have pointed at the contact activation phase as a promising therapeutic target providing an anticoagulant strategy without increas-

ing the risk of bleeding (Jaffer et al (2015); Larsson et al (2014)). A model that incorporates the contact activation system and the coagulation reactions until thrombin formation coupled with a realistic representation of flow dynamics is thus needed. In this article a surface-mediated thrombin production model is presented in a computational hemodynamics framework. The model considers the interaction of the blood flow with the contact activation system and the rest of the blood coagulation cascade; it is detailed in Section 2, together with the numerical method. Furthermore, the model was applied to a device-characteristic flow configuration presented in the experimental work of Taylor et al (2014). To this end, a specific boundary condition was developed to mimic the contact activation at the device surface. This boundary condition was applied to the whole device surface without an a priori knowledge of regions prone to thrombosis. The results discussed in section 3 illustrate the potential of the approach.

2 Materials and Methods

2.1 Governing equations

2.1.1 Fluid dynamics equations

Flow dynamics is described by the incompressible Navier Stokes equations that read

$$\nabla \cdot \mathbf{u} = 0, \quad (1)$$

$$\rho \left(\frac{\partial \mathbf{u}}{\partial t} + \mathbf{u} \cdot \nabla \mathbf{u} \right) = -\nabla p + \mu \nabla^2 \mathbf{u}, \quad (2)$$

where \mathbf{u} is the velocity field, p is the pressure field, ρ stands for the density and μ is the dynamic viscosity (both assumed constant-valued). The blood was considered as a Newtonian fluid (constant viscosity) since the objective of the present study was not focused on the effects due to Non-Newtonian behavior of blood.

2.1.2 Convection-Diffusion-Reaction equations

To account for the coagulation reactions, a set of evolution equations (one for each coagulation factor) is solved. The equation that captures the spatial and temporal evolution of the biochemical species is widely known as the convection-diffusion-reaction equation

$$\frac{\partial C_i}{\partial t} + \nabla \cdot (C_i \mathbf{u}) = \nabla \cdot (D_i \nabla C_i) + R_i, \quad (3)$$

where C_i ($\text{M} = \text{mol L}^{-1} = 10^3 \text{ mol m}^{-3}$) and D_i ($\text{m}^2 \text{ s}^{-1}$) are the molar concentration and diffusion coefficients for each species i , R_i (M s^{-1}) is the reaction source term (computed according to the reactions rates presented in Table 1).

2.2 Coagulation model

A wide variety of models has been proposed to predict thrombin formation inside the blood stream (Anand et al (2003); Leiderman and Fogelson (2011); Biasetti et al (2012)). In those models, coagulation reactions start at the extrinsic pathway by the exposure of TF. In the present work, the presence of an artificial surface in contact with blood is accounted for by including the contact activation system (Basmadjian et al (1997)). For this purpose the kinetic model of Chatterjee et al (2010) is adopted. This set of reactions predicts thrombin production in the absence of exogenous TF and starts the coagulation reactions by the contact activation of factor *XII*. Figure 1 shows a schematic of the coagulation model used for the simulations including the contact activation system and the rest of the coagulation cascade reactions.

In Table 1, the 26 reactions used are listed with their respective reaction rates. The types of reaction kinetics are of first order, second order and Michaelis-Menten. Reaction rates for the different reactions are listed in three different columns according their type. The source terms R_i appearing in Eq. 3 are deduced from the coagulation reactions. It is important to mention that the 53 reaction rates values do not consider the platelet activity that is also reported by Chatterjee et al (2010).

Diffusion coefficients were estimated with the correlation of Young et al (1980). The molecular weight of each chemical species is needed to estimate the diffusion coefficient along with the temperature and the dynamic viscosity. For the present study a temperature of $T = 25$ °C and a dynamic viscosity of $\mu = 3.71 \times 10^{-3}$ Pa s were used. The correlation used considers a partial specific volume of $0.73 \text{ cm}^3 \text{ g}^{-1}$ which is assumed to be common for all the species. The expression proposed by Young et al writes:

$$D = 8.34 \times 10^{-8} (T/\mu M^{1/3}) \quad (4)$$

The diffusion values estimated with Eq. 4 are extremely small (of the order of $10^{-11} \text{ m}^2 \text{ s}^{-1}$). If these values were to be used, numerical instabilities and large diffusion characteristic times would render the convergence to a steady state solution extremely difficult. This problem has been emphasized in studies using numerical models for coagulation. This difficulty is either overcome by refining the mesh or by increasing artificially the diffusion coefficients as in Biasetti et al (2012). Here, we follow the latter approach and multiply all diffusion coefficients by a factor of 1000.

The main objective of this work is to evaluate the potential of the contact activation system to initiate thrombin formation. Consequently, the model did not include inhibitors, TF and fibrin-related reactions that are included in Chatterjee et al (2010). Finally the model assumes an infinite number of binding sites (infinite platelet supply), as in Biasetti et al (2012). The reader is referred to Kuharsky and Fogelson (2001); Anand et al (2003) for a discussion on the role of a finite number of binding sites. **It is important to note that the scope of this article is not to model the complete and complex dynamics of thrombus formation. A more robust model must include the role of anionic phospholipids, platelet adhesion and aggregation as in Leiderman and Fogelson (2011). Other important players for a robust model should be included such as fibrin production (Neeves et al (2010)), coagulation inhibitors (Zhu (2007); Rice et al (2016)) or thrombus growth (solid-fluid interaction) as model by Ngoepe and Ventikos (2016). Such a model may provide a good prediction tool to contribute to the optimization of medical devices.**

2.3 A boundary condition for the contact activation

To model the contact activation of factor *XII*, a wall boundary condition is derived from the species mass balance at the wall where protein adsorption takes place followed by contact activation. The balance is obtained by integrating Eq. 3 over a rectangular control volume Ω (which includes a volume of fluid and a volume of wall, see Fig. 2) of surface Σ . Using the divergence theorem to reformulate the conservative terms and integrating over Ω leads to:

$$\int_{\Omega} \frac{\partial C_i}{\partial t} d\Omega + \int_{\Omega} -R_i d\Omega = \int_{\Sigma} (D_i \nabla C_i) \cdot \mathbf{nd}\Sigma - \int_{\Sigma} C_i \mathbf{u} \cdot \mathbf{nd}\Sigma \quad (5)$$

The reaction source term R_i can be decomposed into the volume (blood-phase) reaction source term $\dot{\omega}_i$ and the surface source term \dot{s}_i multiplied by a Dirac function δ (which is not zero at the device surface). The mass balance becomes:

$$\int_{\Omega} \frac{\partial C_i}{\partial t} d\Omega + \int_{\Omega} -(\dot{\omega}_i + \delta \dot{s}_i) d\Omega = \int_{\Sigma} (D_i \nabla C_i) \cdot \mathbf{nd}\Sigma - \int_{\Sigma} C_i \mathbf{u} \cdot \mathbf{nd}\Sigma \quad (6)$$

The surface Σ can be separated in lateral, inferior and superior surfaces respectively $\Sigma = 2\Sigma_l + \Sigma_{in} + \Sigma_s$. If the height h tends to zero ($h \rightarrow 0$) the volume integrals over Ω and the surface integrals over the lateral surfaces

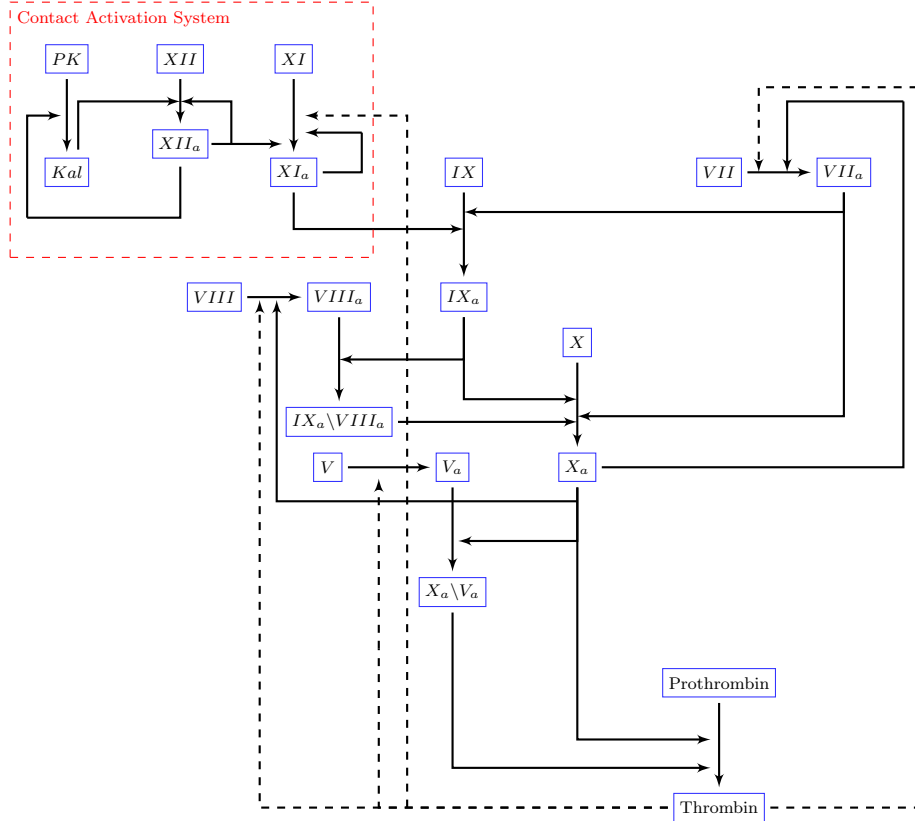


Fig. 1 Schematic of the coagulation reaction network. The kinetic network is inspired from the platelet-plasma model Chatterjee et al (2010) without considering TF, inhibitors and fibrinogen reactions. The dashed lines correspond to the feedback loop reactions related to thrombin.

#	Reaction	$M^{-1}s^{-1}$	s^{-1}	s^{-1}
1	$Xa + VII \rightarrow Xa + VIIa$	$k_1 = 1.3 \times 10^7$		
2	$IIa + VII \rightarrow IIa + VIIa$	$k_2 = 2.3 \times 10^4$		
3	$II + Xa \rightarrow IIa + Xa$	$k_3 = 7.5 \times 10^3$		
4	$IIa + VIII \rightarrow IIa + VIIIa$	$k_4 = 2.0 \times 10^7$		
5	$VIIIa + IXa \leftrightarrow IXa = VIIIa$	$k_5 = 1.0 \times 10^7$		
6	$IXa = VIIIa + X \leftrightarrow IXa = VIIIa = X \rightarrow IXa = VIIIa + Xa$	$k_7 = 1.0 \times 10^8$	$k_6 = 5.0 \times 10^{-3}$	$k_9 = 8.2$
7	$VIIIa \leftrightarrow VIIIa_1 \cdot L + VIIIa_2$		$k_8 = 1.0 \times 10^{-3}$	$k_{11} = 2.2 \times 10^4$
8	$IXa = VIIIa = X \rightarrow VIIIa_1 \cdot L + VIIIa_2 + X + IXa$		$k_{10} = 6.0 \times 10^{-3}$	
9	$IXa = VIIIa \rightarrow VIIIa_1 \cdot L + VIIIa_2 + IXa$		$k_{12} = 1.0 \times 10^{-3}$	
10	$IIa + V \rightarrow IIa + Va$	$k_{14} = 2.0 \times 10^7$		
11	$Xa + Va \leftrightarrow Xa = Va$	$k_{15} = 4.0 \times 10^8$		
12	$Xa = Va + II \leftrightarrow Xa = Va = II \rightarrow Xa = Va + mIIa$	$k_{17} = 1.0 \times 10^8$	$k_{16} = 0.2$	
13	$Xa = Va + mIIa \rightarrow Xa = Va + IIa$	$k_{20} = 1.5 \times 10^7$	$k_{18} = 103$	$k_{19} = 63.5$
14*	$XII \rightarrow XIIa$			
15	$XIIa + XII \leftrightarrow XIIa = XII \rightarrow XIIa + XIIa$	$k_{22} = 1 \times 10^8$	$k_{21} = 5.0 \times 10^{-7} m s^{-1}$	
16	$XIIa + PK \leftrightarrow XIIa = PK \rightarrow XIIa + K$	$k_{25} = 1 \times 10^8$	$k_{23} = 750$	$k_{24} = 3.3 \times 10^{-2}$
17	$XII + K \leftrightarrow XII = K \rightarrow XIIa + K$	$k_{28} = 1 \times 10^8$	$k_{26} = 3.6 \times 10^3$	$k_{27} = 40$
18	$PK + K \rightarrow K + K$	$k_{31} = 2.7 \times 10^4$	$k_{29} = 45.3$	$k_{30} = 5.7$
19	$XI + IIa \leftrightarrow XI = IIa \rightarrow XIa + IIa$	$k_{32} = 1 \times 10^8$	$k_{33} = 5$	$k_{34} = 1.3 \times 10^{-4}$
20	$XIIa + XI \leftrightarrow XIIa = XI \rightarrow XIIa + XIa$	$k_{35} = 1.0 \times 10^8$	$k_{36} = 200$	$k_{37} = 5.7 \times 10^{-4}$
21	$XIa + XI \rightarrow XIa + XIa$	$k_{38} = 3.19 \times 10^6$		
22	$XIa + IX \leftrightarrow XIa = IX \rightarrow XIa + IXa$	$k_{39} = 1.0 \times 10^8$	$k_{40} = 41.0$	$k_{41} = 7.7$
23	$IXa + X \leftrightarrow IXa = X \rightarrow IXa + Xa$	$k_{42} = 1.0 \times 10^8$	$k_{43} = 0.64$	$k_{44} = 7.0 \times 10^{-4}$
24	$Xa + VIII \leftrightarrow Xa = VIII \rightarrow Xa + VIIIa$	$k_{45} = 1.0 \times 10^8$	$k_{46} = 2.1$	$k_{47} = 0.023$
25	$VIIa + IX \leftrightarrow VIIa = IX \rightarrow VIIa + IXa$	$k_{48} = 1.0 \times 10^8$	$k_{49} = 0.9$	$k_{50} = 3.6 \times 10^{-5}$
26	$VIIa + X \leftrightarrow VIIa = X \rightarrow VIIa + Xa$	$k_{51} = 1.0 \times 10^8$	$k_{52} = 210$	$k_{53} = 1.6 \times 10^{-6}$

Table 1 Coagulation reactions. Kinetic parameters and coagulation reactions used in the simulations. Reaction 14 is taken into account only at the surface by means of the wall boundary condition. Parameter k_{21} units ($m s^{-1}$) correspond to a surface reaction, the value was obtained adapting the volume reaction rate from Chatterjee et al (2010) assuming a characteristic length of 1.0 mm.

Σ_l are equal to zero; the inferior surface Σ_{in} collapse with the device wall and the surface reaction source term can be transformed in a surface integral over the device wall thanks to the Dirac function. In addition

the convection fluxes at the device surface are equal to zero (assuming the wall is at rest and impermeable),

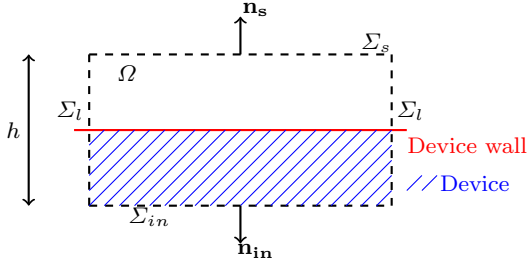


Fig. 2 Mass balance around the device wall. Ω Control of volume, Σ Surface envelope of the control volume, Sub index in , s and l stand for the inferior, superior and lateral surfaces respectively, h height of the control volume.

thus Eq.5 can be rewritten as:

$$-\int_{\Sigma_s} (D_i \nabla C_i) \cdot \mathbf{n}_s d\Sigma_s = \int_{\Sigma_{in}} (D_i \nabla C_i) \cdot \mathbf{n}_{in} d\Sigma_{in} + \int_{\Sigma_{in}} \dot{s}_i d\Sigma_{in} \quad (7)$$

The diffusion flux inside the solid domain is zero since no species is present in the device itself; thus one can write:

$$-\int_{\Sigma_s} (D_i \nabla C_i) \cdot \mathbf{n}_s d\Sigma_s = \int_{\Sigma_{in}} \dot{s}_i d\Sigma_{in} \quad (8)$$

A boundary condition can be obtained by applying Eq. 8 to factor XII_a . The surface source term is obtained assuming an infinitely fast adsorption and an infinite number of binding sites for factor XII , thus the reaction that takes place is the conversion of the near-wall factor XII (indexed by w) to XII_a . Finally the following wall boundary condition is obtained:

$$D_{XII_a} \frac{\partial C_{XII_a}}{\partial n} = -k_s C_{XII_w} \quad (9)$$

where k_s is a material property (surface reaction rate) and the direction n is the normal direction pointing to the blood-phase of the domain. In this study the value published in Chatterjee et al (2010) for the activation of factor XII in a perfectly mixed environment was used as a starting point for k_s . The volume reaction rate was converted to a surface rate using a characteristic length equal to $l = 1$ mm which led to the value of $k_s = 5.0 \times 10^{-7} \text{ m s}^{-1}$. **The characteristic length value was set to match the characteristic size of a batch reactor which correspond to the experimental set up of Chatterjee et al (2010).** A range of values was also considered to investigate the effect of this physical quantity on the results (see section 3).

2.4 Numerical implementation and verification

Equations 1 and 2 were solved with a fourth-order finite-volume method on an unstructured grid, implemented in the in-house YALES2BIO¹ solver. YALES2BIO is based on a massivel parallel finite volume solver for incompressible flows (Moureau et al (2011)) and has been extensively validated for several biomedical applications at micro and macro scale (Chnafa et al (2014b,a); Mendez et al (2014); Sigüenza et al (2017); Chnafa et al (2016); Lanotte et al (2016); Zmijanovic et al (2017)). It uses a spatial fourth-order scheme with an explicit four-step Runge-Kutta scheme in time. The pressure term is handle with the Chorin's projection-correction method. Equation 3 was also solved using a fourth-order scheme in space and time for each species. Several test cases were developed to verify the implementation of Eq. 3 in YALES2BIO. Test cases with reactions of the Michaelis-Menten type (?), as well as first and second order reactions were compared against analytic solutions. Furthermore, the results of the kinetic model introduced by Hockin et al (2002) were reproduced. In this test case the reactions start with an initial condition of exogenous TF. This allows to validate the different types of reactions that are shared by the different coagulation kinetic schemes; for instance, reactions 1 to 13 in Table 1 are shared with the scheme of Hockin et al (2002).

Moreover, a simple 1D diffusive test case involving a volume and a surface reaction (contact activation boundary condition) without convection was specifically designed during the course of this study. In this academical configuration illustrated in Fig. 3, a species A can be either activated at the bottom wall and become A_a (surface reaction rate k_s) or transformed into species B in the flow domain (volume reaction rate k_v), whereas the upper wall acts like an infinite reservoir at concentration $C_A(h) = \alpha$. In the calculations the domain is 2D, with periodic conditions in the directions tangential to the walls. The analytic steady state solution for the concentration of species A reads:

$$C_A(y) = \frac{\alpha e^{\beta(h-y)} (k_s (e^{2\beta y} - 1) + \beta D_A (1 + e^{2\beta y}))}{k_s (e^{2\beta h} - 1) + \beta D_A (1 + e^{2\beta h})} \quad (10)$$

where k_s and k_v are the surface and volume reaction rates, respectively, $\beta = \sqrt{\frac{k_v}{D_A}}$ and h is the channel height. Table 2 shows the three different operating points that were used to verify the results.

¹ <http://www.math.univ-montp2.fr/~yales2bio/>

Cases	k_s m s ⁻¹	k_v s ⁻¹
Case ₁	1.0×10^{-4}	1.0×10^4
Case ₂	1.0×10^{-4}	1.0×10^3
Case ₃	1.0×10^{-2}	1.0×10^2

Table 2 Operating points. The different set of parameters (k_s and k_v) used for the verification of the code. The corresponding steady state solutions are shown in Fig. 3.

Figure 3 shows the steady state solution of species A for both the numerical and analytic cases. An excellent agreement is obtained for all of the operating points.

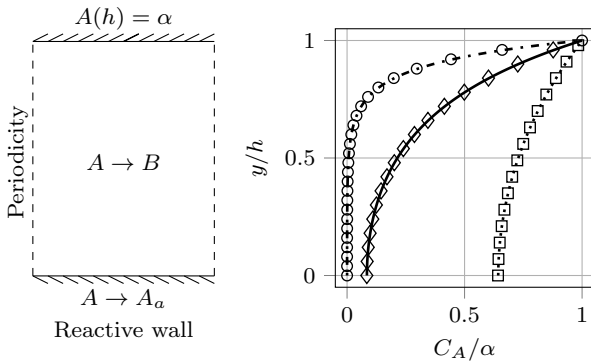


Fig. 3 1D reaction-diffusion test case. $C_A = \alpha = 1.0 \mu\text{M}$, initial volume concentration of all the species $C_i = 0$ M, diffusion coefficient of species $D_A = D_B = 1.0 \times 10^{-2} \text{ m}^2 \text{ s}^{-1}$, channel height $h = 0.01$ m. Numerical results (Case₁ \circ , Case₂ \diamond , Case₃ \square) and analytic Eq. 10 data (Case₁ $\cdots\cdots$, Case₂ — , Case₃ $\cdots\cdots$).

2.5 Backward facing step configuration

Numerical simulations are performed in a backward facing step (BFS) configuration presented in Fig. 4, advancing the set of reactions presented in Table 1. This type of configuration involves a flow separation that several medical devices could feature and which has been related to thrombus formation (Hastings et al (2017); Taylor et al (2014)). The step height $h_s = 2.5$ mm and vessel height $H = 10$ mm match the experimental dimensions presented by Taylor et al (2014).

The inlet and outlet conditions were placed at a distance of $10H$ to avoid boundary effects on the region of interest located downstream of the step: the expected recirculation zone for the flow regime considered (Reynolds number $Re = 430$, based on the inlet channel height and the upstream bulk velocity) is $Xr = 8.9h_s$ according to the results of Kim and Moin (1985). The kinematic viscosity was set to a constant value $\nu = 3.5 \times 10^{-6} \text{ m}^2 \text{ s}^{-1}$.

Boundary and initial conditions. The inlet velocity was set to $U_x = 0.2 \text{ m s}^{-1}$, consistently with the experimental conditions described in Taylor et al (2014). Table 3 shows the initial and inlet boundary conditions factors that were taken from Chatterjee et al (2010) and which correspond to physiological values. The boundary and initial conditions for the rest of the factors were set to zero. One of the most important features of the simulation is the reactive surface boundary condition, Eq. 9. The boundary condition for the contact activation of factor XII was applied at the entire wall of the computational domain (see Fig. 4).

Factor	Concentration (M)
VII	1.0×10^{-8}
VIIa	1.0×10^{-10}
X	1.6×10^{-7}
IX	9.0×10^{-8}
II	1.4×10^{-6}
VIII	7.0×10^{-10}
V	2.0×10^{-8}
XII	3.4×10^{-7}
PK	4.5×10^{-7}
XI	3.1×10^{-8}

Table 3 Initial and inlet factor concentrations. Physiological values used in the simulations taken from Chatterjee et al (2010).

Spatial and temporal resolution. Several grids were used to ensure that the simulations yield results independent from the grid used in the calculation. Table 4 shows the representative cell size and the number of elements used for the computations. **The simulation time step is given by the Courant-Friedrichs-Levy stability condition which is define using the time step Δt , the local velocity field u and the mesh size Δx as $CFL = \frac{u\Delta t}{\Delta x} \leq 1$. The value used in the current simulations is $CFL = 0.9$ which corresponds to a time step of the order 10^{-4} s.**

Grid	Δ_h (μm)	Elements $\times 10^3$
Coarse	70	367
Medium	60	484
Fine	52	646

Table 4 Mesh properties. Δ_h is the representative cell size computed as in Celik et al (2008) and the total number of grid elements (triangles) are displayed.

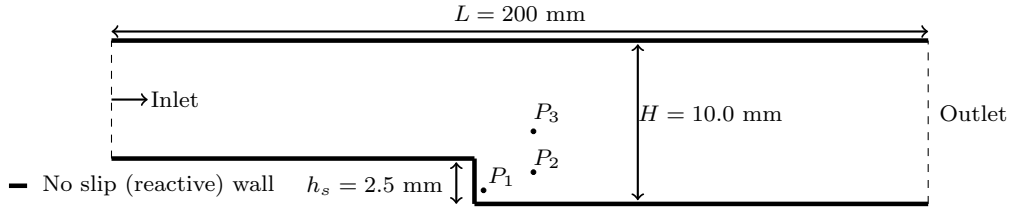


Fig. 4 2D Backward facing step computational domain. P_i are the locations of the probes used in Figs. 5, 7 and Fig. 11 ($P_1 = (0.5, 0.5)$, $P_2 = (4.0, 1.5)$, $P_3 = (4.0, 4.0)$ mm); the step and channel heights match the experimental values of Taylor et al (2014). The thick black line denotes the solid boundary where boundary condition Eq. 9 is applied and activation of factor XII is allowed.

3 Results: Backward facing step

3.1 Flow Dynamics

The velocity field reached a steady state solution before 1.0 s as shown in Fig. 5 for different spatial point probes located inside and outside the recirculation zone.

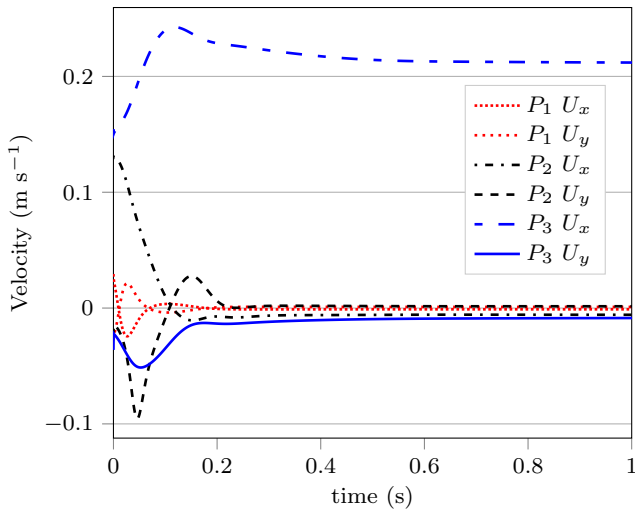


Fig. 5 Temporal evolution of x and y velocity components in different point probes.

Figure 6 shows the steady state velocity field as well as the streamlines that allow the visualization of recirculation region after the step. The reattachment length X_r is in good agreement with the numerical and experimental results published in Kim and Moin (1985); Armaly et al (1983) which lead to $X_r = 8.9h$. The comparison was performed for all the grids used in this study. The percentage error of the coarser mesh was $e_{rel} = 3.1\%$ and for the medium and fine mesh of about $e_{rel} = 2.9\%$ which is a fair approximation considering the main objective of the current study.

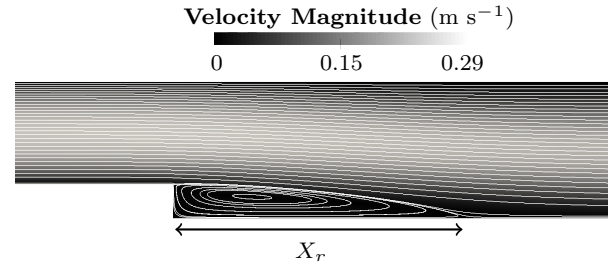


Fig. 6 Velocity magnitude with white stream lines. The reattachment length X_r is shown.

3.2 Coagulation cascade

In order to quantify the outcome of the coagulation cascade, the value of total thrombin is considered ($II_a + 1.2mII_a$ is a quantitative measure of thrombin activity in the system, according to Hockin et al (2002)). First, a mesh convergence study was performed using the mean value of the total thrombin in the computational domain. The methodology published in Celik et al (2008) was used. The convergence grid index is used to quantify the distance of a computed value (simulation result) to the asymptotic value estimated by an extrapolation method using the different levels of discretization. For the finest mesh the convergence grid index obtained was $CGI_{finest} = 0.41\%$ with a relative extrapolated error of $e_{ext} = 0.33\%$, the quantity used for the analysis was the total thrombin concentration value of a point probe inside the recirculation region. These values ensure that the total thrombin concentration field would not substantially change with even a finer mesh. The surface rate used for the mesh convergence study was $k_{21} = 5.0 \times 10^{-4} \text{ m s}^{-1}$, in order to reduce the computational cost of the study.

Figure 7 shows the time evolution of total thrombin at point probes P_1 , P_2 and P_3 (see Fig. 4 for the location of the probes). The time response is characterized by a lag time of about 100 s. Then, a propagation phase is observed until a small peak which evolves into a more stable plateau close to the inlet value of $II = 1.4 \mu\text{M}$.

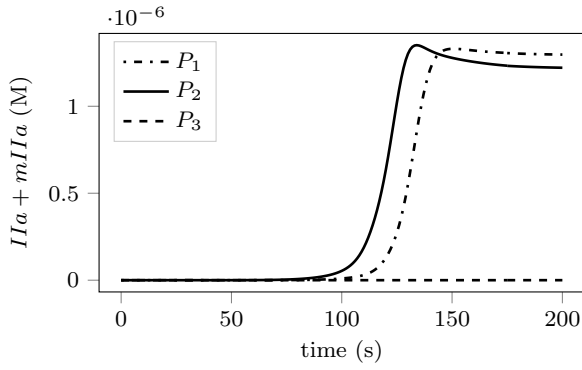


Fig. 7 Time evolution of $II_a + 1.2mII_a$ for each point probe (see Fig. 4). P_1 is near the wall region, P_2 inside the recirculation zone and P_3 outside the recirculation region.

Figure 8 shows the concentration field evolution of total thrombin at different time values. It can be observed that the region of largest total thrombin concentration is located inside the recirculation zone downstream of the step. Large concentrations of total thrombin extend further downstream at the lower wall.

The local concentration of coagulation factors inside the recirculation region is shown in Fig. 9. The plot is extracted along a profile located at the half height of the step (h_s), $y = 1.25$ mm. It can be observed that the largest concentration of total thrombin is located at the step wall.

Thrombin concentration levels at the recirculation region are large enough to form a stable thrombus (Bisetti et al (2012)). Furthermore, the zone with the largest concentration of thrombin align well with the experimental zone in which thrombus is formed (Taylor et al (2014)).

3.2.1 Flow metrics and Contact system activation (WSS vs XII_a , XI_a)

Figure 10 shows a scatter plot of the wall shear stress against the near wall concentrations of factors XII_a and XI_a . The quantities were normalized by the maximum Wall shear stress and maximum concentrations of species XII_a and XI_a . Factor XII_a production is equal in all the range of WSS. In contrast, even though a clear correlation is not observed factor XI_a plot shows that the largest production of factor XI_a is related to small values of WSS.

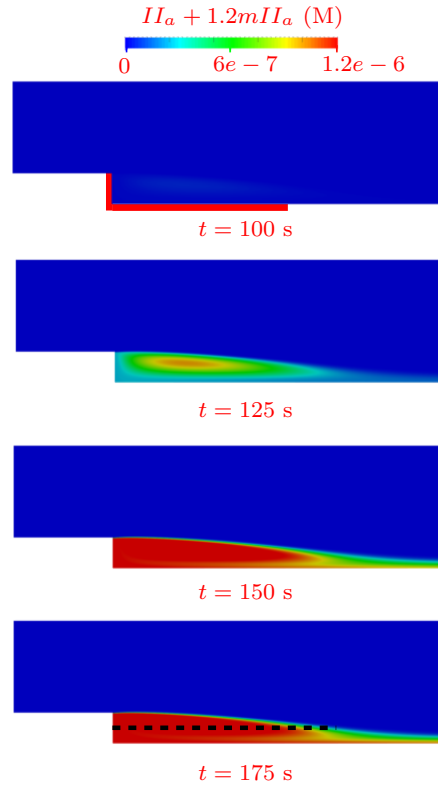



Fig. 8 Total thrombin concentration field at $t = 100, 125, 150$ and 175 s. The black dashed line represents the plot of Fig. 9. The red line is an approximate form the experimental wall region of thrombus formation of Taylor et al (2014). The red line  in the field ($t = 100$) shows an approximates of the experimental zone in which thrombus formation takes place at the wall.

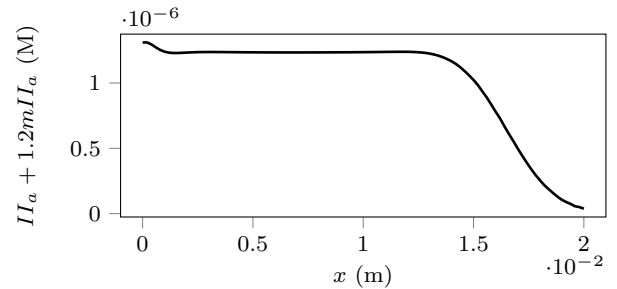


Fig. 9 $II_a + 1.2mII_a$ concentration in the recirculation zone.

3.2.2 Parametric study of the influence of surface kinetics

As already mentioned, there is a lack of reliable data about the surface reaction rate (k_{21} contact activation) and this quantity may depend on the material type. Therefore, to investigate how the outcome of the simulations depends on this parameter, a parametric study was performed. Six values were evaluated in the range $k_{21} = [5.0 \times 10^{-5}, 5.0 \times 10^{-10}]$ m s⁻¹ spanning six orders of magnitude. Figure 11 shows the evolution at point

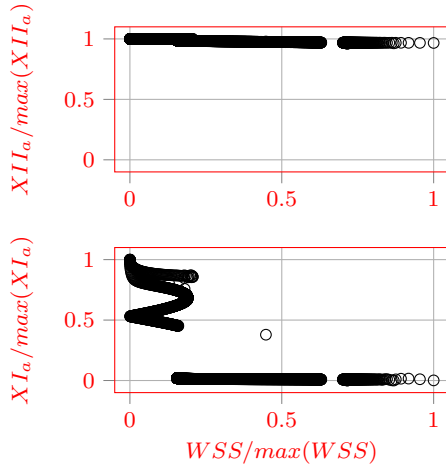


Fig. 10 Scatter plot of wall shear stress and near wall concentrations of factors XII_a and XI_a .

probe P_1 of factors XII_a , XI_a and $II_a + 1.2mII_a$ over time. In addition, inserts in the plots display the variation of specific times of interest with respect to k_{21} . For $II_a + 1.2mII_a$ and XII_a , the inflection point of the time evolution graphs is extracted by fitting a hyperbolic tangent function. For factor XI_a , the insert shows the time at which the maximum concentration is reached. The thrombin generation starts earlier as the parameter k_{21} is increased. However, while five orders of magnitude are explored for the value of k_{21} , the impact on the thrombin generation time is moderate and the dependence appears to be logarithmic. In addition, the total thrombin concentration fields (steady state solution) were compared, showing no significant difference. It can be observed from the evolution of factors XII_a and XI_a that the time delay present in the dynamics of these factors follow the same trend as the one observed for $II_a + 1.2mII_a$. In other words, the initial delay in the activation of factor XII is directly responsible for the delay in thrombin generation. While the influence of k_{21} on the time needed for generation of factor XII_a is very large, this time has to be compared with the total time needed for the rest of the coagulation cascade, which is 10 times larger in the present case. It is important to note that when k_{21} was set to zero the thrombin concentration levels remain zero (not shown).

3.2.3 Parametric study: Influence of factor XII inlet boundary condition.

A parametric study on the inlet concentration of factor XII was performed. Table 5 shows the four different concentration values that were used.

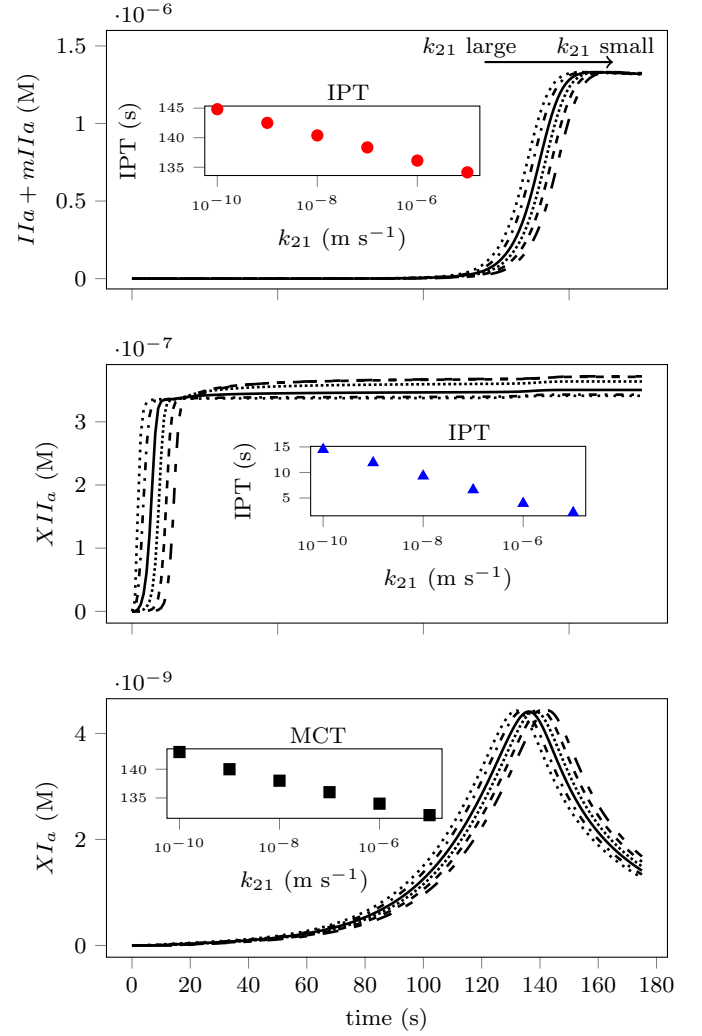


Fig. 11 Time evolution of point probe P_1 for total thrombin (upper), activated factor XII (medium) and activated factor XI (bottom). $k_{21} = 5 \times 10^{-5}$ (.....), $k_{21} = 5 \times 10^{-6}$ (-.-.-), $k_{21} = 5 \times 10^{-7}$ (—), $k_{21} = 5 \times 10^{-8}$ (.....), $k_{21} = 5 \times 10^{-9}$ (- - -), $k_{21} = 5 \times 10^{-10}$ (- - -). The inserts of $II_a + 1.2mII_a$ and XII_a factor show the Inflection Point Time (IPT) for every k_{21} value. For factor XI_a , the insert displays the maximum concentration time (MCT) as a function of k_{21} .

Case	XII (μM)
1	0.306
2	0.272
3	0.17
4	0.102

Table 5 Factor XII inlet concentrations used in the parametric study.

Figure 12 shows the time evolution of point probe P_1 of factors XII_a , XI_a and $II_a + 1.2mII_a$. The results show longer lag times for thrombin propagation as the boundary concentration is decreased. An interesting phenomenon is seen in factor XI_a evolution in

which the maximum production of this factor is increased as factor XII concentration is reduced. This behavior could be explained by a lower activation of factor XI due to factor XII_a . Then, factor XI_a is influenced by a quicker activation due to factor II_a (reaction 19) leading to higher concentrations of XI_a . The difference on factor XII_a is marked by different plateau values equal to the inlet boundary condition values.

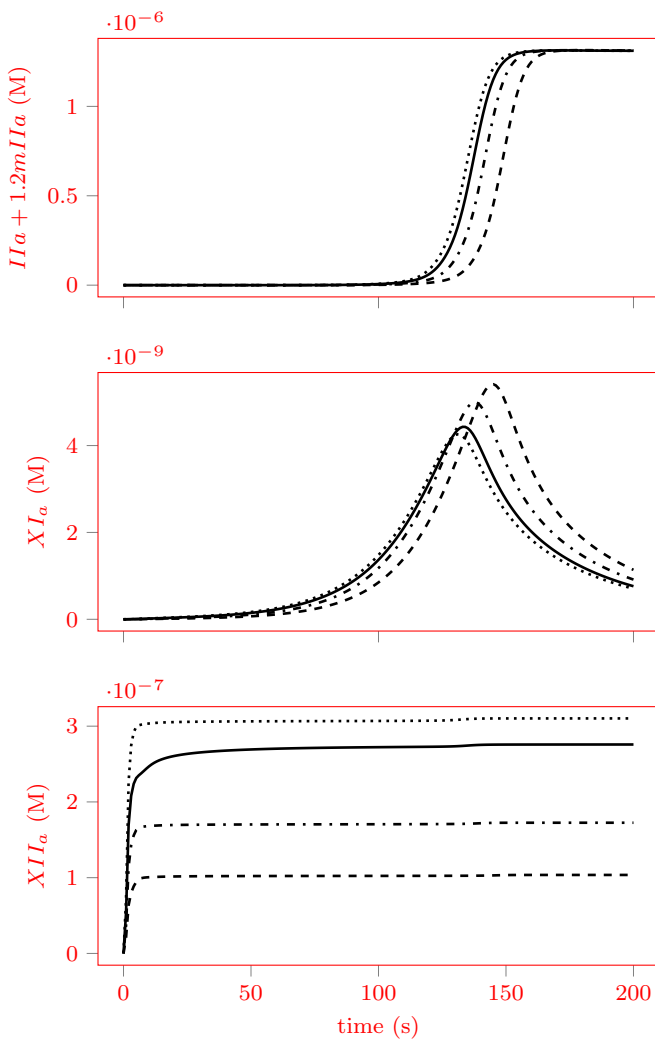


Fig. 12 Time evolution of point probe P_1 for total thrombin (upper), activated factor XII (medium) and activated factor XI (bottom). $XII_{90\%} = 0.306 \mu M$ (---), $XII_{70\%} = 0.272 \mu M$ (-·-·-), $XII_{50\%} = 0.17 \mu M$ (—), $XII_{30\%} = 0.102 \mu M$ (·····).

4 Discussion and Conclusion

Previous studies have modeled device-related thrombosis with an approach focussing on platelet activity (Goodman et al (2005); Taylor et al (2016)). However, the contact activation system is a key component of the thrombotic network (Larsson et al (2014); Jaffer et al (2015)) which up to date has not been included in a complete model of thrombus formation. The current model aims to serve as a first step towards the integration of the contact activation in a complete macroscopic thrombus formation model specific to medical devices. The current model was applied to a backward facing step configuration typical of medical devices.

One of the main features of the model is that it allows the initiation of the coagulation reactions without an a priori knowledge of the thrombotic zone. The results show that a significant amount of thrombin is generated in the recirculating region behind the backward facing step. This could be explained by comparing the characteristic residence and chemical times. Large residence time at the recirculating regions enhances the thrombin production reactions. Qualitatively, the model leads to higher total thrombin concentrations in regions where the thrombus formation was observed experimentally. The results also show a relation between small values of wall shear stress and near wall concentrations of factor XI_a in contrast to near wall concentrations of factor XII_a that is present all along the device surface.

Large diffusion coefficient values ($D_i \sim 10^{-8} \text{ m}^2 \text{ s}^{-1}$) were used to reduce the computational cost of our simulations following Biasseti et al (2012). Figure 13 shows the maximal total thrombin concentration inside the recirculation region for three different orders of magnitude of D_i . It can be seen from the figure that reducing the diffusion coefficient value increases the concentration inside the recirculation region. The potential of the current model to produce thrombin is underestimated, using the real diffusion value would increase or maintain the production observed in our simulations.

An interesting feature of the present model is that it includes a material property k_{21} (typical to each medical device) which is a novel feature for thrombus predictive models representing the kinetics of the contact surface reaction. A parametric study was performed on k_{21} showing a moderate influence of this parameter on the propagation phase of the total thrombin generation at the recirculation zone. The effect of parameter k_{21} will most probably increase if inhibition reactions are taken into account. However, the results of the parametric study are still interesting showing that reducing or increasing the surface reaction rate may delay or speed

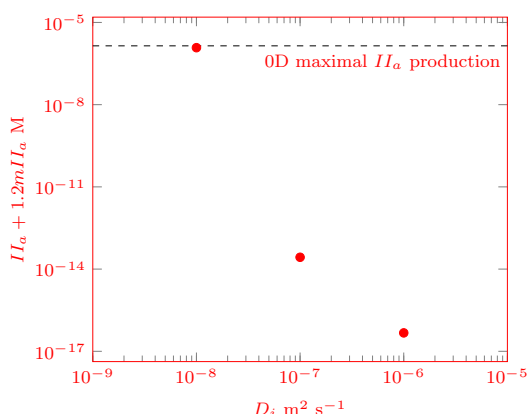


Fig. 13 Maximal total thrombin concentration inside the recirculation region for three orders of magnitude of the diffusion coefficients ($D_i \sim 10^{-8}, 10^{-7}, 10^{-6} \text{ m}^2 \text{ s}^{-1}$).

up the generation of thrombin. The parametric study on the inlet boundary condition concentration of factor XII is similar to the study on k_{21} for the total thrombin evolution. In contrast factor XI_a evolution is influenced in its magnitude and lag time to the propagation phase.

Acknowledgements We are grateful to the CONACyT, Mexico scholarship and the LabEx Numev (convention ANR-10-LABX-20) for their financial support. Drs. Vincent Moureau and Ghislain Lartigue from CORIA laboratory, and the SUCCESS scientific group are acknowledged for providing the YALES2 solver which constitutes the basis of the YALES2BIO tool. Professor Jean-François Schved and MD. Muriel Giansily from the University Hospital of Montpellier are thanked for helpful discussions about the biological aspects of thrombosis. This work was performed using HPC resources from GENCI-CINES (Grants 2016-c2015037194 and 2017-A0020307194) and with the support of the High Performance Computing Platform HPC@LR.

Conflict of Interest: The authors declare that they have no conflict of interest.

References

Alemu Y, Girdhar G, Xenos M, Sheriff J, Jesty J, Einav S, Bluestein D (2010) Design optimization of a mechanical heart valve for reducing valve thrombogenicity - a case study with aortic valve. *Am. Soc. Artif. Intern. Org.* 56(5):389–396

Anand M, Rajagopal K, Rajagopal KR (2003) A model incorporating some of the mechanical and biochemical factors underlying clot formation and dissolution in flowing blood. *J. Theor. Med.* 5:183–218

Anand M, Rajagopal K, Rajagopal KR (2008) A model for the formation, growth, and lysis of clots in quiescent plasma. a comparison between the effects of antithrombin iii deficiency and protein c deficiency. *J. Theor. Biol.* 253:725–738

Armaly BF, Durst F, Pereira JCF (1983) Experimental and theoretical investigation of backward-facing step flow. *J. Fluid Mech.* 127:473–496

Basmadjian D, Sefton MV, Baldwin SA (1997) Coagulation on biomaterials in flowing blood: Some theoretical considerations. *Biomaterials* 18:1511–1522

Biasseti J, Spazzini PG, Swedenborg J, Gasser TC (2012) An integrated fluid-chemical model toward modeling the formation of intra-luminal thrombus in abdominal aortic aneurysms. *Front. Physiol.* 3(266)

Celik IB, Ghia U, Roache PJ, Freitas CJ, Coleman H, Raad PE (2008) Procedure for estimation and reporting of uncertainty due to discretization in CFD applications. *J. Fluids Eng.* 130, article id 078001

Chan MY, Weitz JI, Merhi Y, Harrington RA, Becker RC (2009) Catheter thrombosis and percutaneous coronary intervention: fundamental perspectives on blood, artificial surfaces and antithrombotic drugs. *J. Thromb. Thrombol.* 28:366–380

Chatterjee MS, Denney WS, Jing H, Diamond SL (2010) Systems biology of coagulation initiation: Kinetics of thrombin generation in resting and activated human blood. *PLoS Comp. Biol.* 6(9)

Chnafa C, Mendez S, Moreno R, Nicoud F (2014a) The Cardio-Circulatory System : from Modeling to Clinical Applications, Springer, chap Using image-based CFD to investigate the intracardiac turbulence

Chnafa C, Mendez S, Nicoud F (2014b) Image-based large-eddy simulation in a realistic left heart. *Comput. Fluids* 94:173–187

Chnafa C, Mendez S, Nicoud F (2016) Image-based simulations show important flow fluctuations in a normal left ventricle: What could be the implications? *Ann. of Biomed. Eng.* 44(11):3346–3358

Fogelson AL (1992) Continuum models of platelet aggregation: Formulation and mechanical properties. *SIAM J. Appl. Math.* 52(4):1089–1110

Fogelson AL, Guy RD (2008) Immersed-boundary-type models of intravascular platelet aggregation. *Comput. Meth. Appl. Mech. Eng.* 197:2087–2104

Fogelson AL, Nieves KB (2015) Fluid mechanics of blood clot formation. *Ann. Rev. Fluid Mech.* 47(1):377–403

Furie B, Furie BC (2008) Mechanisms of thrombus formation. *New Eng. J. Med.* 359:938–949

Goodman PD, Barlow ET, Crapo PM, Mohammad SF, Solen KA (2005) Computational model of device-induced thrombosis and thromboembolism. *Ann. of Biomed. Eng.* 33:780–797

Gorbet MB, Sefton MV (2004) Biomaterial-associated thrombosis: roles of coagulation factors, complement, platelets and leukocytes. *Biomaterials* 25:5681–5703

Gregory K, Basmadjian D (1994) An analysis of the contact phase of blood coagulation: Effects of shear rate and surface are intertwined. *Ann. of Biomed. Eng.* 22:184–193

Hastings SM, Ku DN, Wagoner S, Maher OK, Deshpande S (2017) Sources of circuit thrombosis in pediatric extracorporeal membrane oxygenation. *Am. Soc. Artif. Intern. Org.* 63(1):86–92

Hellums JD (1994) 1993 Whitaker lecture: Biorheology in thrombosis research. *Ann. of Biomed. Eng.* 22:445–455

Hockin MF, Jones KC, Everse SJ, Mann KG (2002) A model for the stoichiometric regulation of blood coagulation. *J. Biol. Chem.* 277(21):18,322–18,333

Jaffer IH, Fredenburgh JC, Hirsh J, Weitz JI (2015) Medical device-induced thrombosis: what causes it and how can we prevent it? *J. Thromb. Haemost.* 13(Suppl. 1):72–81

Jesty J, Yin W, Perrotta P, Bluestein D (2003) Platelet activation in a circulating flow loop: combined effects of shear stress and exposure time. *Platelets* 14(3):143–149

- Kim J, Moin P (1985) Application of a fractional-step method to incompressible Navier-Stokes equations. *J. Comput. Phys.*59:308–323
- Kroll MH, Hellums JD, McIntire LV, Schafer AI, Moake JL (1996) Platelets and shear stress. *Blood*88(5):1525–1541
- Kuharsky AL, Fogelson AL (2001) Surface-mediated control of blood coagulation: the role of binding site densities and platelet deposition. *Biophys. J.*80:1050–1074
- Lanotte L, Mauer J, Mendez S, Fedosov DA, Fromental JM, Clavería V, Nicoud F, Gompper G, Abkarian M (2016) Red cells' dynamic morphologies govern blood shear thinning under microcirculatory flow conditions. *Proc. Natl Acad. Sc. USA*113(47):13,289–13,294
- Larsson M, Rayzman V, Nolte MW, Nickel KF, Björkqvist J, Jms A, Hardy MP, Fries M, Schmidbauer S, Hedenqvist P, Broom M, Pragst I, Dickneite G, Wilson MJ, Nash AD, Panousis C, Renné T (2014) A factor xiiia inhibitory antibody provides thromboprotection in extracorporeal circulation without increasing bleeding risk. *Sci. Transl. Med.*6(222)
- Leiderman K, Fogelson AL (2011) Grow with the flow: A spatial-temporal model of platelet deposition and blood coagulation under flow. *Math. Med. Biol.*28:47–84
- Mehra MR, Stewart GC, Uber PA (2014) The vexing problem of thrombosis in long-term mechanical circulatory support. *J. Heart Long Transplant.*33:1–11
- Mendez S, Gibaud E, Nicoud F (2014) An unstructured solver for simulations of deformable particles in flows at arbitrary Reynolds numbers. *J. Comput. Phys.*256(1):465–483
- Moureau V, Domingo P, Vervisch L (2011) Design of a massively parallel CFD code for complex geometries. *Comp. Rend. Méc.*339(2-3):141–148
- Neeves KB, Illing DAR, Diamond SL (2010) Thrombin flux and wall shear rate regulate fibrin fiber deposition state during polymerization under flow. *Biophys. J.*98:1344–1352
- Ngoepe MN, Ventikos Y (2016) Computational modelling of clot development in patient-specific cerebral aneurysm cases. *J. Thromb. Haemost.*14(2):262–272
- Nobili M, Sheriff J, Morbiducci U, Redaelli A, Bluestein D (2008) Platelet activation due to hemodynamic shear stresses: Damage accumulation model and comparison to in vitro measurement. *Am. Soc. Artif. Intern. Org.*54(1):64–72
- Piatti F, Sturla F, Marom G, Sheriff J, Claiborne TE, Slepian MJ, Redaelli A, Bluestein D (2015) Hemodynamic and thrombogenic analysis of a trileaflet polymeric valve using a fluid-structure interaction approach. *J. Biomech.*48(13):3650–3658
- Rice NT, Szlam F, Varner JF, Bernstein PS, Szlam AD, Tanaka KA (2016) Differential contributions of intrinsic and extrinsic pathways to thrombin generation in adult, maternal and cord plasma samples. *PLoS One*11(5):e0154,127
- Seo JH, Abd T, George RT, Mittal R (2016) A coupled chemo-fluidic computational model for thrombogenesis in infarcted left ventricles. *Am. J. Phys.*310(11):H1567–H1582
- Shadden SC, Hendabadi S (2013) Potential fluid mechanic pathways of platelet activation. *Biomech. Model. Mechanobiol.*12:467–474
- Sigüenza J, Mendez S, Nicoud F (2017) How should the optical tweezers experiment be used to characterize the red blood cell membrane mechanics? *Biomech. Model. Mechanobiol.*16:1645–1657
- Sorensen EN, Burgreen GW, Wagner WR, Antaki JF (1999) Computational simulation of platelet deposition and activation: I. model development and properties. *Ann. of Biomed. Eng.*27:436–448
- Taylor J, Witmer K, Neuberger T, Craven B, Meyer R, Deutsch S, Manning KB (2014) In vitro quantification of time dependant thrombus size using magnetic resonance image and computational simulations of thrombus surface shear stresses. *J. Biomech. Eng.*136(7)
- Taylor JO, Meyer RS, Deutsch S, Manning KB (2016) Development of a computational model for macroscopic predictions of device-induced thrombosis. *Biomech. Model. Mechanobiol.*15(6):1713–1731
- Yazdani A, Li H, Humphrey JD, Karniadakis GE (2017) A general shear-dependent model for thrombus formation. *PLoS Comp. Biol.*13(1):e1005,291
- Young ME, Carrood PA, Bell RL (1980) Estimation of diffusion coefficients of proteins. *Biotechnol. Bioeng.*22(5):947–955
- Zhu D (2007) Mathematical modeling of blood coagulation cascade: kinetics of intrinsic and extrinsic pathways in normal and deficient conditions. *Blood. Coagul. Fibrinolysis.*18:637–646
- Zmijanovic V, Mendez S, Moureau V, Nicoud F (2017) About the numerical robustness of biomedical benchmark cases: Interlaboratory FDA's idealized medical device. *Int. J. Numer. Meth. Biomed. Eng.*33(1):e02,789:1–17